Title	Accurate anisotropy recovery from fluorophore mixtures using Multivariate Curve Resolution (MCR)
Author(s)	Casamayou-Boucau, Yannick; Ryder, Alan G.
Publication Date	2017-11-22
Publication Information	Casamayou-Boucau, Yannick, & Ryder, Alan G. (2018). Accurate anisotropy recovery from fluorophore mixtures using Multivariate Curve Resolution (MCR). Analytica Chimica Acta, 1000, 132-143. doi: https://doi.org/10.1016/j.aca.2017.11.031
Publisher	Elsevier
Link to publisher's version	https://doi.org/10.1016/j.aca.2017.11.031
Item record	http://hdl.handle.net/10379/15843
DOI	http://dx.doi.org/10.1016/j.aca.2017.11.031

Accurate anisotropy recovery from fluorophore mixtures using Multivariate Curve Resolution (MCR).

Yannick Casamayou-Boucau and Alan G. Ryder.*
Nanoscale BioPhotonics Laboratory, School of Chemistry, National University of Ireland, Galway, Galway, Ireland.
* Corresponding author: **Email:** alan.ryder@nuigalway.ie, **Phone:** +353-91-492943.
Postal address: Nanoscale Biophotonics Laboratory, School of Chemistry, National University of Ireland, Galway, University Road, Galway, Ireland.

Abstract: Anisotropy resolved multidimensional emission spectroscopy (ARMES) provides valuable insights into multi-fluorophore systems like proteins that have complex overlapping emission bands. The method combines multidimensional fluorescence, anisotropy, and chemometrics to facilitate the differentiation of fluorophores with very similar emission properties. Here, we address the critical issue of standardizing the chemometric methods required to accurately extract spectral and anisotropy information from fluorophore mixtures using two standard sample sets: perylene in glycerol, and a mixture of Erythrosin B and Phloxine B with overlapping emission but different anisotropies.We show for the first time how to accurately model component anisotropy using Multivariate Curve Resolution (MCR) from data collected using total synchronous fluorescence scan (TSFS) and Excitation Emission Matrix (EEM) measurement methods.

These datasets were selected to avoid the presence of inner filter effects (IFE) or F€orster resonance energy transfer (FRET) that would depolarize fluorescence emission or reduce data tri-linearity. This allowed the non-trilinear TSFS data to yield accurate component anisotropy data once modelled using the correct data augmentation strategy, however, the EEM data proved to be more accurate once optimal constraints (non-negativity and correspondence among species) were employed. For perylene (S2) and Phloxine B which both have very weak anisotropy (<0.06), while the spectral recovery was excellent, the modelled anisotropy values were reasonably accurate (±20% of the real value) because of large relative noise contributions. However, for perylene (S1) and Erythrosin B which have large (>0.2) anisotropies, bilinear and trilinear EEM models built using a total tri-linearity constraint, yielded solutions without any rotational ambiguities and very accurate (±4% of real value) anisotropy values. These sample systems thus provide simple and robust test systems for validating the spectral measurement and chemometric data analysis elements of ARMES.

Keywords: Fluorescence, Anisotropy, Multidimensional, Standards, Chemometrics.

1. Introduction.

Protein analysis by intrinsic fluorescence is useful because it is non-invasive and also preserves the structure and behavior of protein native states [1-5]. The multiple fluorophores usually present in proteins are however generally in close proximity (<5 nm) and thus interact photophysically *via* Förster resonance energy transfer (FRET), and electron transfer quenching by peptide bonds. Furthermore, variable solvent exposure and inner filter effects (IFE) also cause a complex emission [6, 7]. To fully explore this complex emission space, multidimensional fluorescence spectroscopy (MDF) measurement techniques like excitation-emission matrix (EEM) [8] and Total Synchronous Fluorescence Scan (TSFS) [9] are used and both have specific advantages and disadvantages. TSFS is for example almost twice as fast as EEM because it only measures the spectral region where $\lambda_{em} > \lambda_{ex}$ [10], and it also avoids 1st order Rayleigh scatter contamination which is an important consideration for anisotropy measurements [1]. Both methods provide more information about the multiple fluorophores [11, 12] present in proteins, and are dependent on critical parameters that govern emission. These parameters, determined by protein structure, are the location, separation, and orientation of the fluorophores or other photophysically active molecules (*e.g.* quenchers), which govern FRET and quenching processes.

A major problem with fluorescence spectroscopy of multi-fluorophore proteins is that extensive spectral overlap makes spectral interpretation difficult. Multivariate curve resolution (MCR) [13-16], and parallel factor analysis (PARAFAC) [17-19] can be used to identify the spectral contributions of individual constituents from MDF data, which can then be associated with specific fluorophore emission and processes. However, these methods work well only when MDF data is not, or minimally affected by scatter, IFE, or FRET. Rayleigh and Raman scatter also cause problems as they are non-bilinear elements, negatively impacting the deconvolution of EEM [20-23]. While scatter can be corrected with a variety of methods, it would be much more advantageous to avoid the strongest 1st order Rayleigh using TSFS measurements.

Unfortunately, one drawback with TSFS data modelling is its complex data structure which arises from the dependence of the emission measured at the offset ($\Delta\lambda$) with λ_{ex} [24]. Whereas in EEM (of well-behaved samples like a single ideal fluorophore) the intensity of the fluorescence signal changes as a function of both the excitation or emission wavelength, the spectra profile tends to remain the same in both dimensions (*i.e.* the shape of the excitation and emission spectra do not vary). EEM is thus considered to be trilinear because both excitation and emission are highly reproducible spectral orders [25]. In TSFS, a change in $\Delta\lambda$ induces a change in spectral profile, which means that TSFS does not behave tri-linearly [26], which has a negative impact on MCR or PARAFAC modelling. The situation becomes more complex if IFE or FRET are present. IFE [27] breaks the linearity between fluorescence intensity and concentration, and can also drastically distort EEM profiles. Because this distortion can vary from sample to sample, the reproducibility of excitation and emission spectral orders is greatly reduced, which breaks the tri-linearity of EEM data [23, 28-31]. In TSFS data, IFE also affects spectral profiles and cause misinterpretations [32]. Similarly, large deviation from tri-linearity are encountered in the presence of FRET [33] particularly when chromophores/fluorophores are in close proximity (<10 nm).

This is the author version, final accepted draft, but not proof corrected.

However, even with careful chemometric analysis of good quality data (scatter free or corrected, IFE corrected, and FRET free), fluorophore emission can remain unresolvable, so one needs to measure other properties (*e.g.* lifetime, anisotropy) to enable fluorophore resolution. Combining anisotropy with MDF [34] enabled the differentiation and quantification of fluorophores with similar emission properties in complex mixtures, based on their rotational speed and hydrodynamic volume, and thus the molecular size, or for macromolecules the mobility/flexibility of the constituent fluorophores. ARMES a 4D measurement (λ_{ex}, λ_{em}, I, r), exploits this and can provide an additional layer of information that enables the differentiation of fluorophores with very similar emission properties.

In the first ARMES studies, using TSFS measurements and polymer thin film polarizers (TFP) [34, 35], we observed that multi-fluorophore albumin proteins generated complex *aniso*-TSFS (excitation wavelength (λ_{ex}) × wavelength offset ($\Delta\lambda$) × anisotropy (r)) plots that were diagnostic of both protein identity and structure. TFP however, do not transmit below ~290 nm, which did not permit the collection of the complete intrinsic protein fluorescence originating from Tyrosine and Tryptophan. TFP also caused the excitation maxima of the recovered components to be both red-shifted and reshaped, compared to non-polarized spectra [35]. While this distortion compensated for the lack of tri-linearity in TSFS data, it also distorted the recovered excitation profiles which often appeared to have dual bands, an artefact caused by the TSFS data structure.

The ARMES measurement wavelength range can be extended using polarizers with better UV transmittance and enable the acquisition of data in the important tyrosine/tryptophan region [36]. Polarizer efficacy was confirmed using a perylene standard which has two different emitting states with different fundamental anisotropies of 0.4 (S_1) and –0.2 (S_2) [37, 38], and the measured anisotropy was significant in viscous glycerol solution: 0.197 and –0.031 ± 0.002 at 25°C [39]. However, the use of UV transmitting filters also resulted in the elimination of the spectral reshaping previously observed in TSFS measurements [35] which has consequences in terms of data structure.

Before applying ARMES to the analysis of proteins, it was first necessary to investigate and standardize the chemometric methodology to be used. In particular, one has to determine if it was possible to extract using curve resolution methods (here MCR) accurate excitation and emission, scores and profiles, and therefore anisotropy values for individual fluorophores using either TSFS or EEM data. To do this we also had to determine the optimal data augmentation procedure to ensure recovery of reliable spectral profiles and scores from MCR. A second facet of the study was to determine if TSFS measurements made using a dual wire grid polarizer (dWGP) could still be analyzed as demonstrated previously [35] which required an investigation into how to deal with trilinear (EEM) and non-trilinear (TSFS) data. We also had to ascertain what were the optimal constraints to use, to produce accurate solutions without rotational ambiguities. This was important in some measurement situations where excess light scatter cannot be avoided and thus TSFS will be more suitable measurement, for example in turbid media like bioreactors.

Here we studied two systems: a major/minor fluorophore mixture (perylene in glycerol, used to validate hardware performance, [36]), and second where there were two fluorophores of similar molecular size (Erythrosin B and Phloxine B) with overlapping emission spectra of

This is the author version, final accepted draft, but not proof corrected.

the same intensity but different anisotropies. These samples had minimal IFE and FRET, which ensured data tri-linearity and minimized unwanted depolarization effects.

2. Materials and Methods

2.1 Materials: Perylene, Erythrosin B (EB), and Phloxine B (PB) were purchased from Sigma-Aldrich and used as received without further purification. Glycerol (spectrophotometric grade ≥ 99.5%) was purchased from Acros Organics. A 1 µM stock solution of perylene in 100% glycerol was prepared, and then diluted to obtain 0.2, 0.5, and 0.8 µM solutions. Erythrosin B (~ 6 µM) and Phloxine B (~ 0.6 µM) stock solutions were prepared in HEPES buffer (pH = 7.2, 25 °C) which were then combined to prepare solutions of mixed fluorophore concentrations (Table S-7, SI). All concentrations were chosen to minimise IFE. There was no particular reason for selecting a closed system ($\sum C_i = 100\%$) for the EB:PB mixtures. However, this is a worst case example for MCR because the different concentration profiles are linearly dependent (if one decreases, the other one increases, or both decrease or increase at same time), which can create rank deficiency. One therefore can evaluate the quality of the MCR models if they can deal with this issue.

2.2 Instrumentation and data collection: Fluorescence data were measured in triplicate at 25°C from solutions in 0.4×1 cm pathlength quartz cuvettes (Lightpath Optical, UK) using an Eclipse Fluorescence Spectrophotometer (Agilent) fitted with dWGP [36] and a thermostatted multi-cell holder. Samples were thermally equilibrated for several minutes prior to measurements. For perylene, EEM data were collected for $\lambda_{ex}/\lambda_{em}$ range of 230–470/420-530 nm (2 nm steps) with 5 and 10 nm excitation/emission slit widths. TSFS measurements were collected using λ_{ex} = 230–470 nm and $\Delta\lambda$ intervals of 20–210 nm (2 nm steps). EEM data of the Xanthene dyes were collected using 10/10 nm slits widths and $\lambda_{ex}/\lambda_{em}$ range of 470–570/500-650 nm (2 nm steps). For each sample, four different polarized spectra were collected: vertical-vertical (VV), vertical-horizontal (VH), horizontal-vertical (HV) and horizontal-horizontal (HH). Spectra were not corrected for instrument response. The anisotropy (*r*) at each $\lambda_{ex}/\lambda_{em}$ wavelength pair was calculated using the $r = (\mathbf{I_{VV}} - \mathbf{G} \times \mathbf{I_{VH}})/(\mathbf{I_{VV}} + \mathbf{2} \times \mathbf{G} \times \mathbf{I_{VH}})$ formula [1], where G (=I_{HV}/I_{HH}) corrected for instrument response.

2.3 Data analysis: Chemometric analyses were performed using MATLAB (ver. 7.0.1), using either PLS_Toolbox4.0® or MCR_ALS 2.0 toolbox [40] for implementation of trilinear constraints. MCR-ALS was selected for data analysis to ensure continuity with previous studies [34, 35, 41] although PARAFAC [18] could also be applied to this type of data. TSFS data were organized by λ_{ex} (mode 1), $\Delta\lambda$ (mode 2), and sample (mode 3), same as EEM where mode 2 was λ_{em}. The number of factors, were assessed using SVD. Spectral decomposition was performed on augmented matrix datasets and unless otherwise stated, for TSFS the "concentration" mode corresponded to "λ_{ex} × sample" and the "spectral" mode to $\Delta\lambda$. This was the same for EEM except that the "spectral" mode was λ_{em}. Spectral deconvolution was performed using MCR-ALS [42] and estimation of rotational ambiguities were performed using MCR-BANDS [43]. Separate models were built for each polarization setting once initial estimates had been obtained using SIMPLISMA [44]. A non-negativity constraint was used on both concentration and pure spectra profiles, as well as normalization of the spectral profiles to equal length (Euclidean) to avoid intensity ambiguities between components. In all cases,

This is the author version, final accepted draft, but not proof corrected.

models converged with fewer than 100 iterations (due to the simplicity of the dataset). A similarity index (SimI), was used to rapidly compare EEM/TSFS spectra or anisotropy maps [45]. SimI between two matrices X_1 and X_2 (e.g. EEM or TSFS of dimensions I x J, discrete data points) was calculated using the following equation:

$$SimI = 1 - \lambda \frac{\sqrt{\sum_{i=1}^{I} \sum_{j=1}^{J} p^2{}_{x1-x2}}}{\sqrt{\sum_{i=1}^{I} \sum_{j=1}^{J} p^2{}_{x1+x2}}}$$

λ was a penalty parameter, used to set a detectable limit of variance between X1 and X2. In these calculations it was set to 4 which corresponds to 5% variance in the multidimensional fluorescence data and was proven quite adequate. p_{x1-x2} and p_{x1+x2} are elements of (X1-X2) and (X1 + X2) respectively. The closer SimI value was to one, the more alike the two matrices X_1 and X_2 were.

3. Results and Discussion.

3.1 Perylene data: presence of a fluorescent impurity

A simple standard sample set (perylene, varying concentration in glycerol, [46]) was used as the initial test to establish if either TSFS and EEM, could accurately extract component anisotropy using MCR modelling. These samples contained a weak fluorescent impurity (Figure 1) which originated from the solvent. This was confirmed by overlapping the EEM spectrum of pure glycerol with perylene (Fig. S-1, *Supplemental Information*, SI). Glycerol is known to contain organic fluorescent impurities [47-49]. While the use of more highly purified solvents and blank subtraction is recommended to remove the influence of minor solvent impurities and Raman scatter, it may not always be feasible. However, we felt that it was also important to demonstrate that chemometric modelling could also recover weakly fluorescing components such as impurities (which could originate from fluorophore or glassware contamination). Especially, as weak fluorescing components can also be encountered during protein analysis.
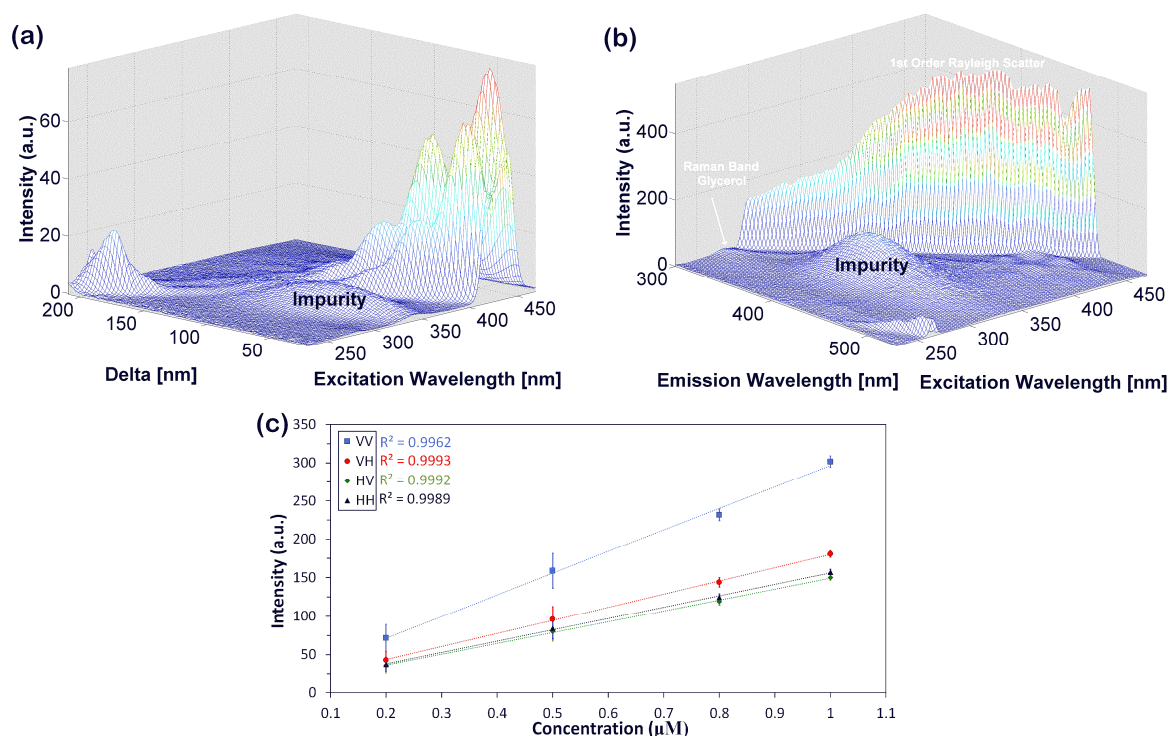
Figure 1: *(a)* VV-TSFS spectrum of a 0.2 μM Perylene solution, showing the impurity signal at $\lambda_{ex}/\Delta\lambda$ = 328/70 nm; *(b)* VV-EEM spectrum of glycerol (blank) collected using a higher detector gain (PMT voltage of 800V instead of 600V); *(c)* Fluorescence intensity vs concentration of perylene in 100% glycerol, for each polarization setting. Error bars were obtained over 3 replicates.

In this TSFS data, 1st order Rayleigh scattering was intrinsically eliminated but Raman scattering from the solvent was present, even though it was too weak to be observed with the experimental conditions used. The Raman spectrum of glycerol (mainly O-H stretching mode at ~3400 cm^{-1}) was only measurable from blank measurements in the VV orientation (highly polarized scatter) using a higher gain on the detector (PMT voltage of 800V instead of 600V). But even here, the Raman band of glycerol was < 7% of the intensity of the impurity signal (Figure 1), which means that it could be eliminated as a source of error.

Rayleigh scatter was therefore the major non-bilinear element to be considered here for the EEM data of perylene because the 1st order band overlapped the S$_1$ emission and 2nd order the S$_2$ emission. Due to this extensive overlap, classical interpolation could not correct sufficiently well for anisotropy studies. We therefore used modelling of shifted scatter by PCA or PARAFAC [20] for Rayleigh scatter removal which was proven to produce accurate anisotropy measurements over a much wider emission range [36]. If the Rayleigh was not removed then MCR modelling produces very erratic results (Figure S-2, SI).

3.2 MCR Analysis of polarized TSFS perylene data:

The TSFS trilinear-like behaviour observed by Groza *et al.* [35] which was due to TFP induced spectral reshaping, enabled the use of column wise augmentation (CWA), $\Delta\lambda \times (\lambda_{ex} \times$ samples), for MCR-ALS analysis. This however contradicted the rank dependency normally observed in this type of augmentation [24]. This reshaping was eliminated once the dWGP were used since the full emission spectra was now obtained. Modelling this dWGP-TSFS

This is the author version, final accepted draft, but not proof corrected.

perylene dataset (for all four polarization configurations) using CWA required five components which was obviously too many (scores and loadings are shown Figure S-4/S-5, SI). Instead of fitting/generating a pure perylene spectrum, the components appeared as combinations/rearrangements of the different vibronic bands associated with each electronic transition (Figures S-3, SI) and this effect was directly related to the non-bilinear behaviour of TSFS data [26].

Even though all the CWA-MCR-TSFS models explained >90% of the variance (Table S-1, SI) and components were recovered without any rotational ambiguities (table S-2, SI) the Lack of Fit (LOF) was too high, which is symptomatic of non-bilinear data trying to be fitted with a bilinear model. LOF [42] corresponds to the difference between the input data (D) and the data reproduced by MCR-ALS: C x S^T. In this equation, d_{ij} correspond to an element of D and e_{ij} of the model residuals.

$$lack\ of\ fit\ (\%) = 100\ \sqrt{\frac{\sum_{i,j} e^2{}_{ij}}{\sum_{i,j} d^2{}_{ij}}}$$

Increasing component number (to 9 or 13 suggested by SVD local minima) decreased LOF to ~ 2% and increased the explained variance to >99% in all modes. However, this did not make chemical sense, because the recovered components (not shown) all overlapped. In addition, the anisotropies calculated from five pure profiles extracted from each MCR model were not constant along Δλ (for example component 1 and 5, Figure S-6, SI). Therefore, we can conclude that CWA was not satisfactory. Row-wise augmentation would be expected to give similar kind of resolution, as λ$_{ex}$ × (Δλ × samples) with concentration and spectral modes that were co-dependant.

Table 1: Perylene in Glycerol MCR best model results. Percentage of variance captured by each MCR model component (Fit %X). Each model convered with ~ 100 iterations, and were built using variety of constraints *1)*. normalization, *2)*. non-negativity, *3)*. unimodality, and *5)*. total tri-linearity. For SWA-TSFS and EEM models, non-negativity was applied on both concentration and spectral modes, and normalization was applied on spectral modes. Unimodality and tri-linearity were applied on augmented mode for SWA-TSFS and EEM models respectively.

SWA-TSFS MCR model (constraints 1,2,3)				
Comp	HH (%X)	HV (%X)	VH (%X)	VV (%X)
1	99.82%	99.86%	99.89%	99.86%
2	0.12%	0.10%	0.07%	0.12%
Sum	99.94%	99.96%	99.96%	99.98%
Lack of Fit	2.40%	1.95%	2.02%	1.34%
EEM MCR model (constraints 1,2,5)				
Comp	HH (%X)	HV (%X)	VH (%X)	VV (%X)
1	99.77%	99.78%	99.84%	99.80%
2	0.19%	0.17%	0.12%	0.15%
Sum	99.96%	99.95%	99.96%	99.95%
Lack of Fit	2.09%	2.12%	1.93%	2.26%

This is the author version, final accepted draft, but not proof corrected.

The correct way to unfold a TSFS dataset for MCR-ALS is along the sample direction (samples $\times$ ($\lambda_{ex} \times \Delta\lambda$)) as only this allowed generation of an independent and equal rank for both directions of the unfolded matrix (samples and $\lambda_{ex} \times \Delta\lambda$) [24]. This rank should also equal to the real number of fluorophores in solution if there was no FRET or IFE effects present. Using this sample wise augmentation (SWA) approach, the unfolded TSFS matrix behaved bilinearly and MCR-ALS modelling of this SWA-TSFS perylene data only required two components (Table 1). A first attempt using only normalization and non-negativity constraints (Table S-5, SI), yielded one component for perylene (98% explained variance), and a second for the fluorescence impurity (~2% variance). However, component two appeared to be a composite of impurity emission (centred at $\lambda_{ex}/\lambda_{em}$ 328/398 nm) mixed with perylene emission (Figure S-11, SI). To improve resolution, stricter constraints were applied by adding unimodality to component two, using the average implementation and a tolerance of 1.1, because the second component behaved unimodally (Figure 1a). Consequently, LOF increased from ~1.3% to ~ 1.9%, however, compared to CWA, the results were indicative of a true, bilinear structure in the augmented TSFS dataset.

Resolution was improved (Figures S-12/S-13, SI) and the first component (perylene) now explained >99.8% of the variance, and the second component <0.2% (similar to EEM, Table 1). The second component was however only partially resolved (inset S-12) and not equally resolved in all samples (as shown by the decreasing scores in Fig. S-13, SI). It seems likely that some of the impurity emission is still present in the 1st component (Fig. S-15, SI). This model, however, enabled the recovery of accurate perylene anisotropy values (Table S-6, Figure S-14, SI) which was important because TSFS may be the only practical ARMES measurement method for highly scattering samples. However, the main issue with this model was the presence of rotational ambiguities in the solution (especially for impurity, Table 2), which cannot be reduced (by application of trilinear constraint for example) showing the limitations of SWA-TSFS.

Table 2: Estimation of component rotational ambiguities by MCR-BANDS using various constraints: *1).* Normalization, *2).* Non-negativity, *3).* Unimodality, and *5).* Total tri-linearity, for TSFS and EEM MCR models.

SWA-TSFS MCR model.								
1,2,3	**Component 1 (~ 99.8%)**				**Component 2 (~ 0.1%)**			
	HH	**HV**	**VH**	**VV**	**HH**	**HV**	**VH**	**VV**
f_n initial	0.998	0.998	0.999	0.998	0.035	0.031	0.026	0.035
f_n max	0.998	0.998	0.999	0.998	0.145	0.136	0.132	0.172
f_n min	0.937	0.896	0.950	0.884	0.035	0.136	0.026	0.035
f_n max-f_n min	0.061	0.102	0.049	0.114	0.110	0.105	0.106	0.137
EEM MCR model								
1,2,5	**Component 1 (~ 99.8%)**				**Component 2 (~ 0.2%)**			
	HH	**HV**	**VH**	**VV**	**HH**	**HV**	**VH**	**VV**

This is the author version, final accepted draft, but not proof corrected.

f_n initial	0.992	0.991	0.994	0.995	0.044	0.041	0.034	0.038
f_n max	0.992	0.991	0.994	0.995	0.044	0.041	0.034	0.038
f_n min	0.992	0.991	0.994	0.995	0.044	0.041	0.034	0.038
f_n max-f_n min	0.000	0.000	0.000	0.000	0.000	0.000	0.000	0.000

The loss of tri-linearity because of the WGP increased UV transmittance meant that CWA was not applicable to TSFS data. SWA unfolding on the other hand was mathematically correct for MCR-ALS [26], and enabled the separation of perylene and impurity once the correct constraints were applied. Even if the 2nd component only partially recovered the impurity, we were able to accurately reconstruct anisotropy values of Perylene for both excited states. Although SWA permitted bilinear decomposition of augmented TSFS data, the data was still not trilinear. This meant that neither PARAFAC nor trilinear constraints could be applied, and one therefore must deal with presence of rotational ambiguities in the model solutions.

3.3 MCR-ALS models on EEM data.

For EEM data, a key consideration was implementation of a tri-linearity constraint during MCR modelling to ensure accurate and unambiguous recovery of all components. The development of mathematical multilinear constraints [25] made it possible to reproduce the inner trilinear structure [50] of PARAFAC in MCR-ALS, by implementing tri-linearity as an optional constraint. The trilinear constraint in MCR-ALS forces the resolved pure profiles to behave the same in all C or S^T matrices. In fact, because this constraint can be implemented separately on each species [42], it allows a certain degree of flexibility for cases varying from pure bi-linearity to complete tri-linearity [51]. Within the trilinear case, the profiles can be further constrained by synchronisation, which can correct for spectral shifts and force the profiles to appear at the same positions for all samples. Tri-linearity constraints are powerful because if the dataset is suitable then this constraint can ensure resolution of pure and unambiguous profiles [50, 52]. However, fluorescence dataset requirements for its use are demanding [25] as they must be free of scatter, IFE, and FRET. The Rayleigh corrected polarized-EEM datasets of perylene in glycerol fulfils the tri-linearity criteria as shown by the plots of maximum fluorescence intensity against concentration obtained for each polarized dataset (Figure 1c) which are all highly linear (r^2>0.99). This is further confirmed by the anisotropy measurements (Table 4) which were constant (and agreed with the literature [39]) at all concentrations, indicating the absence of depolarization processes such as IFE or FRET.

We also verified that the dataset was not unnaturally forced to fit the trilinear constraint by following how the MCR model fit evolved as we progressed from the use of a simple bilinear constraint, to the use of a partial trilinear (shape) constraint, and finally a total trilinear (shape + synchronisation) constraint were applied (Table 3). If the percentage of variance explained R^2 and the lack of fit LOF were constant, then one can reasonable consider that the data structure was suitable for using a trilinear constraint. Here all the polarised perylene/glycerol data were found suitable. It is useful to note that PARAFAC would have been a good alternative to MCR with the tri-linear constraint for modelling this type of data. However, here we also needed to compare bilinear with trilinear models, and MCR offers the

This is the author version, final accepted draft, but not proof corrected.

advantage to switch between bilinear to partial tri-linear and total trilinear cases which may be important in the future for modelling more complex emission systems like multi-fluorophore proteins.

Table 3: Evolution of R^2 and LOF of MCR models applied to CWA-EEM polarized data, when: *1)*. Normalization, *2)*. Non-negativity, *3)*. Bilinear, *4)*. Partially trilinear, and *5)*. Total trilinear constraints were applied.

	R^2 (total variance explained)				LOF (lack of fit)			
	HH	**HV**	**VH**	**VV**	**HH**	**HV**	**VH**	**VV**
1,2,3	99.96%	99.95%	99.97%	99.95%	1.96%	1.95%	1.83%	2.19%
1,2,4	99.96%	99.95%	99.96%	99.65%	2.10%	2.12%	1.95%	2.28%
1,2,5	99.96%	99.95%	99.96%	99.95%	2.09%	2.12%	1.93%	2.26%

Table 4: Real and modelled (from EEM-MCR, constraints 1,2,5) averaged anisotropy values calculated for each concentration, for $\lambda_{ex}/_{em}$ (S_2) = 240-270/430-520 nm and $\lambda_{ex}/_{em}$ (S_1) = 370-460/430-520 nm.

	Real anisotropy $\pm$ **STD**		Modelled anisotropy $\pm$ **STD**	
	S_2	S_1	S_2	S_1
0.2 μM	-0.034 ± 0.010	0.204 ± 0.015	-0.031 ± 0.012	0.201 ± 0.014
0.5 μM	-0.026 ± 0.004	0.202 ± 0.007	-0.030 ± 0.005	0.202 ± 0.007
0.8 μM	-0.030 ± 0.004	0.192 ± 0.004	-0.037 ± 0.002	0.194 ± 0.003
1 μM	-0.035 ± 0.004	0.204 ± 0.002	-0.027 ± 0.002	0.205 ± 0.002
Av/std	-0.031 ± 0.004	0.201 ± 0.005	-0.031 ± 0.004	0.201 ± 0.005

As expected, MCR modelling of EEM data required two components (Table 1) with explained variance for the second impurity component (0.2%) slightly higher than SWA-TSFS where impurity was only partially recovered (Figure S-12, SI). This recovered second component was purer, entirely recovered as shown by the normalized-averaged excitation and normalized emission of the spectral loadings (Figure 2 a/b for HH, others are shown in Fig. S-8, SI). The use of a total trilinear constraint during ALS optimization significantly improved impurity resolution. This can be shown by comparison with the results from a model run only with non-negativity and normalization constraints (Fig. S-7, SI). In addition, the tri-linearity constraint also ensured that both components were resolved without any ambiguities (Table 2) whereas the use of only non-negativity and normalization constraints resulted in some rotational ambiguities, particularly with the weak second component (table S-3). This was also a big improvement compared to SWA-TSFS model.
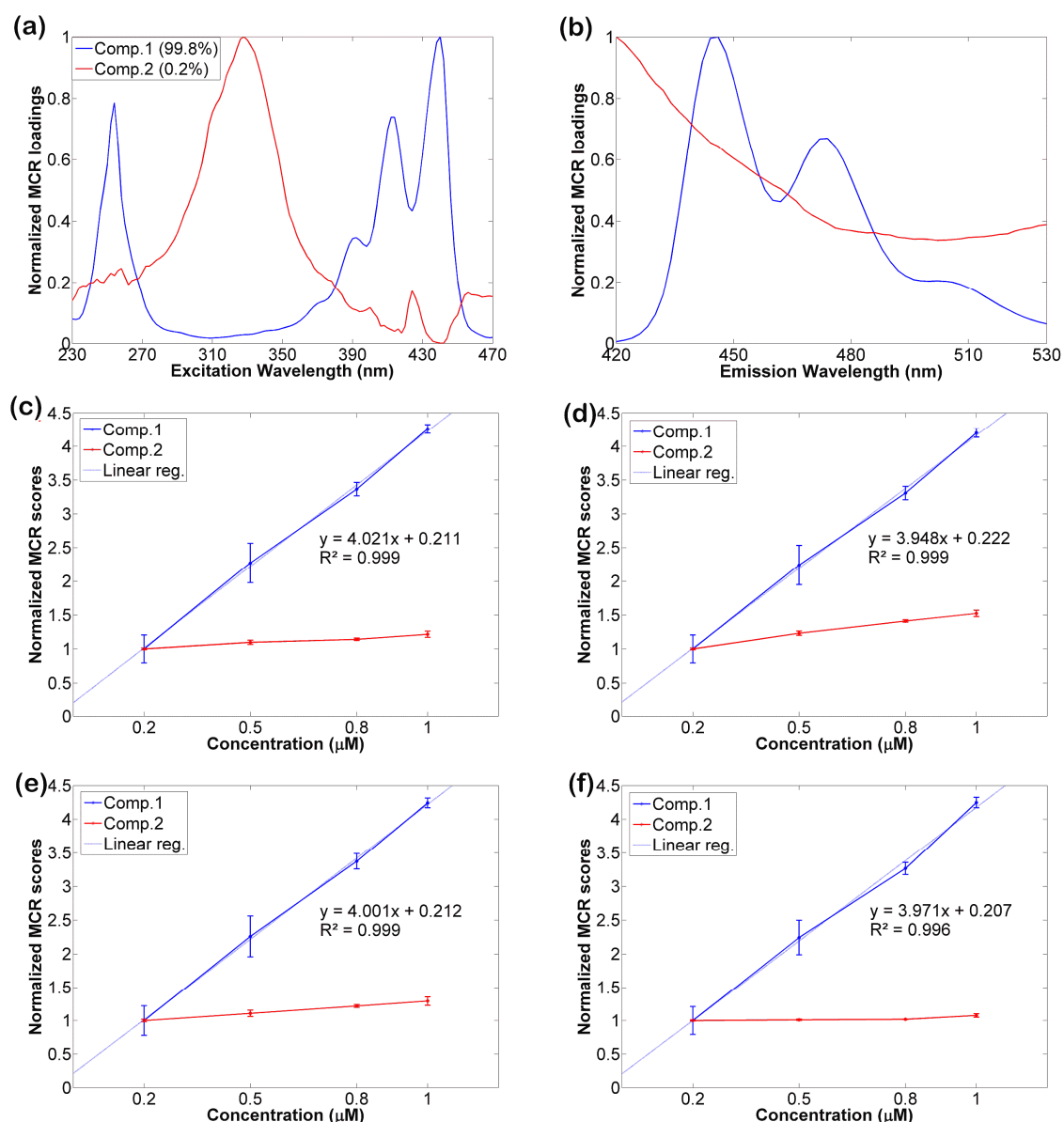
Figure 2: **(top, a/b)** Normalized excitation (averaged across all samples, left) and emission (right) profiles obtained for each pure component after MCR modelling of the HH polarized EEM datasets. Note: emission axis range in (b) was selected to better show only the perylene emission.; **(bottom)** MCR scores (scaled to 1st sample) obtained for HH (c), HV (d), VH (e), and VV (f) polarized data. Models obtained using: 1). normalization, 2). non-negativity constraints and 5) total trilinear constraints.

The normalised MCR scores (Figure 2 c-f) which represent the relative concentration of each extracted fluorophore show that the first component scores increase very linearly ($r^2 > 0.99$ for all) with perylene concentration. The scores for component 2 are not constant with perylene concentration, and tend to increase particularly in HV and VH. Due to the very low fluorophore concentrations for both components, there are small chances it is FRET. This is also confirmed by Fig.S-9 SI showing that the fluorescence intensity of the impurity was ~ constant with perylene concentration, for each polarization setting. The observed increase was probably due to incomplete resolution in the excitation spectra (<270 nm and >390 nm) where there was small, yet significant overlap with perylene (Fig.2, Fig S-8) particularly in the orthogonal HV, VH configurations.

3.4 Perylene anisotropy modelling

Finally, using the spectral profiles for each component generated from the best four polarized-EEM models, we calculated the anisotropy and generated an overlay plot which compared the real anisotropy to the modelled anisotropy (Figure 3). This showed that the modelled and real anisotropy values were in excellent agreement along both excitation and emission directions for both excited states. Once averaged across the entire S_1 and S_2 bands (Table 4), the real and modelled anisotropy values were identical within experimental error.
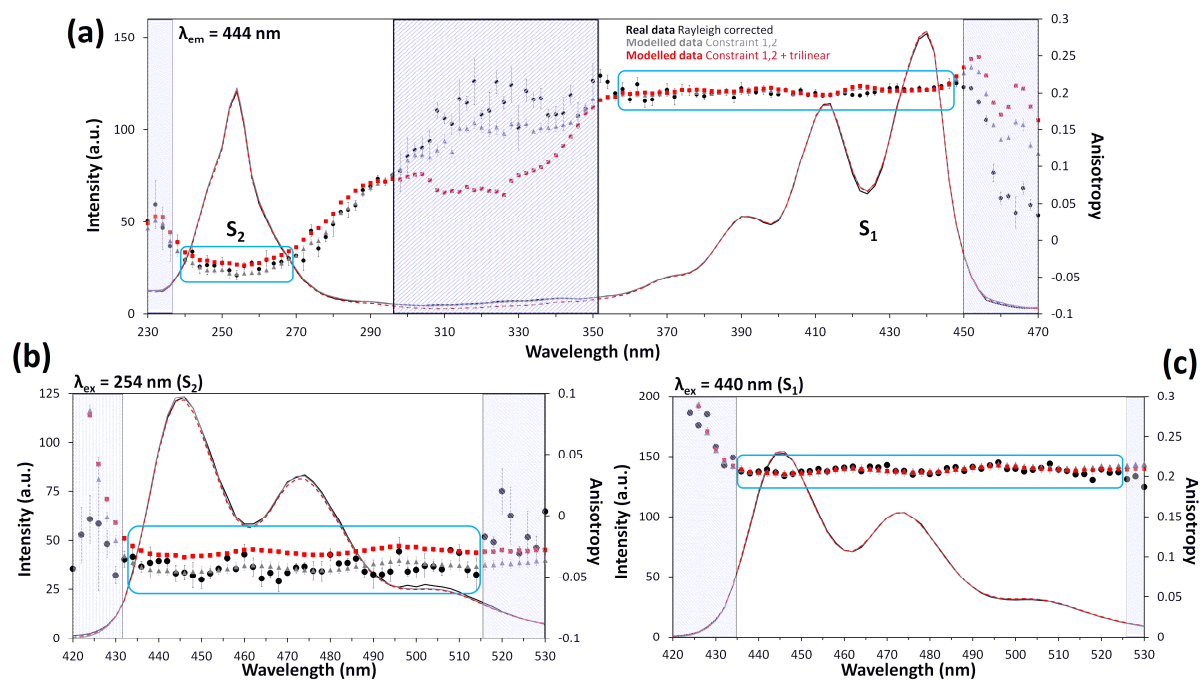

Figure 3: Overlay of HH-EEM excitation (A, λ_{em} = 444 nm) and emission (B, λ_{ex} = 254 nm & C, λ_{ex} = 440 nm) spectra (all corrected for 1st and 2nd order Rayleigh scatter) from perylene (1 μM) in glycerol with corresponding anisotropy values: black = real data; grey = modelled using constraints 1 & 2; red = modelled using 1, 2, & trilinear constraints. The blue boxed areas show the regions of most reliable anisotropy data. The shaded areas represent areas of low fluorescence intensity and thus unreliable anisotropy data.

The only big difference between the real and modelled data in the excitation spectra were observed between the two electronic states (λ_{ex} = 300–350 nm), where mostly noise was present. In the emission spectra (Figure 3b), a small discontinuity between the real and modelled spectra was observed at ~495–515 nm, which corresponded to the location of second order Rayleigh scatter. Therefore, it was possible that a small amount of residual scatter was present in the data, which would explain the slightly higher anisotropy values obtained in this region. Both bilinear and trilinear models accurately retrieved perylene anisotropy for the S_1 state, and the bilinear model was in slightly better agreement with the real anisotropy values (table S-4 *vs* table 4). This was also observed in the S_2 region, where the trilinear model slightly overestimated the anisotropy. In this particular case, perylene, where Rayleigh scatter was

almost perfectly removed, the bilinear model worked better because it offered more flexibility to the spectra to best fit the data and reproduce the exact anisotropy. In contrast the trilinear model restrained the spectral shape more strongly which lead to the discrepancy observed. This was in contrast with cases where residual scatter (noise) in the data can affect the shape of the resolved spectra, and where trilinear models can help to fix this issue (*i.e.* fluorophore mixtures). However, the differences were small and are only really significant when the magnitude of the anisotropy is small, such as with the S_2 state here. Trilinear models have other advantages, such as avoiding rotational ambiguities and preserving a common spectral shape for same component across samples, which is of more practical significance in cases where the components have similar emission intensities. This advantage was seen in case of the impurity, where the trilinear model better resolved the impurity profile. Modelling of this second very weak (~0.2% variance) impurity component was more challenging because the signal to noise ratio was poor. From the excitation (Fig. S-10A, SI) and emission (Fig. S-10B, SI) spectra, it seemed that within the band (λ_{ex} = 290-350 nm), both bilinear and trilinear models were able to accurately reproduce the real anisotropy $r = 0.310 \pm 0.024$.

3.5 Fluorophore mixture modelling

To further validate this chemometric methodology for accurate anisotropy recovery via MCR, we needed to examine a case where there were two fluorophores with overlapping emissions of near equal intensity but with different anisotropies. This is more representative of the situation existing in proteins. We used a mixture of Erythrosin B (~ 6 µM) and Phloxine B (~ 0.6 µM), analysed in HEPES buffer at pH 7.2 (Table S-7, SI) and 25°C. These concentrations yielded equivalent fluorescence intensities and minimized IFE [53]. In addition, the short lifetimes (for example 75 ps for Erythrosin B in water [54]) of these fluorophores should further minimize depolarization effects. The absorbance and the uncorrected fluorescence EEM spectra (Figure 4) of Phloxine B and Erythrosin B show that there is a small degree of IFE for EB, expected because of the relatively high absorbance (~ 0.18) for 6 µM EB compared to (~ 0.019) for 0.6 µM PB.
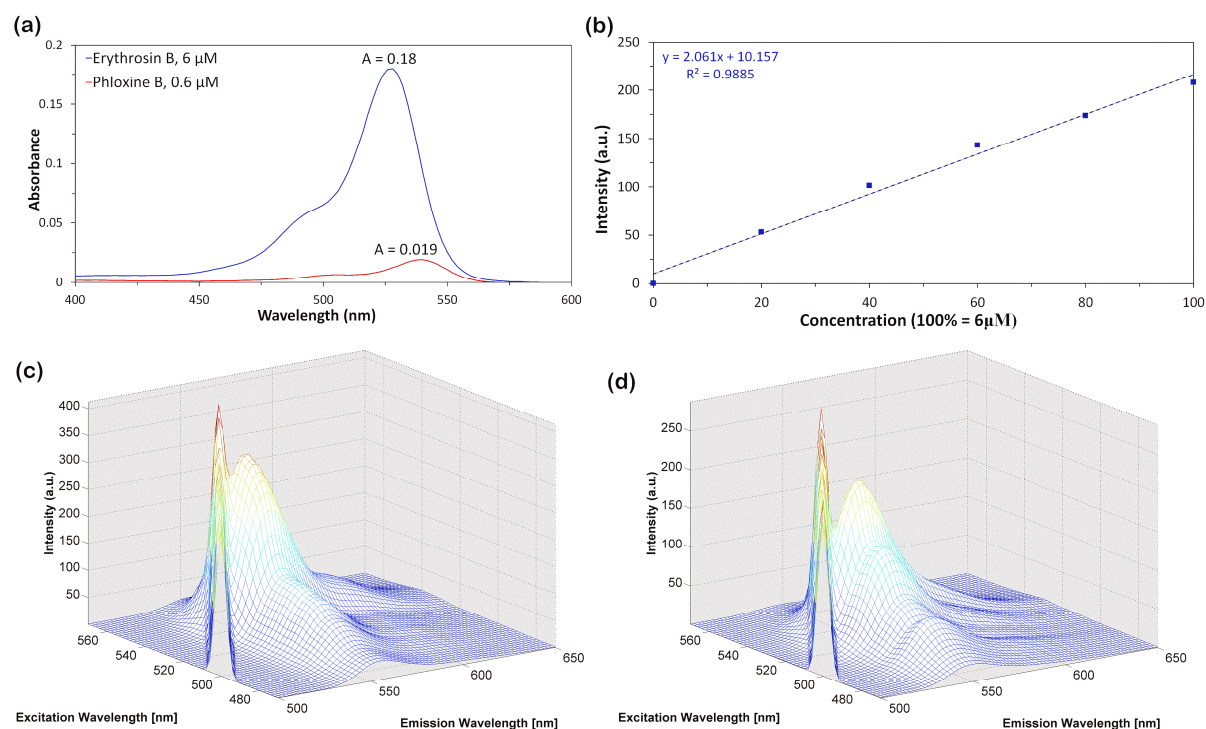
Figure 4: (a) UV-Vis spectra of 6 µM Erythrosin B and 0.6 µM Phloxine B; **(b)** Plot of maximum fluorescence intensity versus Erythrosin B concentration; EEM spectra of: **(c)** 6 µM Erythrosin B and **(d)** 0.6 µM Phloxine B. All data were averaged from three replicate measurements.

MCR modelling was then implemented using a similar process as for perylene. The EEM data were Rayleigh scatter corrected (Fig.S-16, SI) and then MCR models were built for each polarization setting using CWA data. Initial estimates were obtained using the pure fluorophore spectra. Non-negativity constraint was used on both concentration and pure spectra profiles, as well as normalization to equal length (Euclidean) in order to avoid intensity ambiguities between components. If no other constraints were applied, two components were resolved, but the components were not pure (Fig. S-17, SI). To solve this issue, we implemented the "*correspondence among species*" option available in MCR-ALS 2.0 toolbox for multiset data structures [40], to inform the model about the presence/absence of both species in the augmented mode. This constraint, which extends the concept of selectivity and local rank constraints to a multiset structure, is particularly useful for known chemical systems, as it reduces the rotational ambiguities of the solution [52] and helps the algorithm to converge quicker to the correct solution.

Table 5: Estimation of rotational ambiguities per component for the best EB-PB-EEM-MCR MCR model. Built using 1: normalization, 2: non-negativity, 5: total trilinearity and 6: correspondence among species.

1,2,5,6	Component 1				Component 2			
	HH	**HV**	**VH**	**VV**	**HH**	**HV**	**VH**	**VV**
f_n **initial**	0.453	0.448	0.436	0.596	0.754	0.756	0.768	0.628
f_n **max**	0.453	0.448	0.436	0.596	0.754	0.756	0.768	0.628

This is the author version, final accepted draft, but not proof corrected.

f_n **min**	0.453	0.448	0.436	0.596	0.754	0.756	0.768	0.628
f_n **max-f_n min**	0.000	0.000	0.000	0.000	0.000	0.000	0.000	0.000

Rotational ambiguities were removed by application of constraints 1,2,6 (table S-8, SI). However, we noted that the spectral profiles (especially for PB) were not well resolved, with presence of a small shift in PB, and noise in the loadings (due to residual scatter in data, particularly for the VV, Fig S-18 SI). This negatively impacted the accuracy of the calculated anisotropy (SI table S-9). The trilinear constraint was applied to rectify the problem, and this improved the shape of recovered components (less noise and no band shifts), which produced more accurate component anisotropy values (Table 7).

Table 6: Evolution of R^2 and LOF of the MCR models for the EB-PB-EEM data using combinations of constraints: normalization (1), non-negativity (2), total trilinear (5), and correspondence among species (6). Percentage of variance captured by each MCR model component (Fit %X) for 100 iterations.

EB-PB-EEM MCR model (constraints 1,2,6)				
Comp	HH (%X)	HV (%X)	VH (%X)	VV (%X)
1	26.94%	26.84%	24.36%	48.43%
2	73.01%	73.11%	75.60%	51.45%
Sum	99.95%	99.95%	99.96%	99.88%
Lack of Fit	2.32%	2.29%	2.10%	3.45%
EB-PB-EEM MCR model (constraints 1,2,5,6)				
Comp	HH (%X)	HV (%X)	VH (%X)	VV (%X)
1	26.42%	25.97%	24.35%	47.32%
2	73.37%	73.85%	75.45%	52.35%
Sum	99.79%	99.82%	99.80%	99.67%
Lack of Fit	4.57%	4.25%	4.45%	**5.73%**

LOF increased with application of the trilinear constraint (Table 6) and was probably due to the presence of residual scatter in the EEM. Wider excitation slits (10 versus 5 nm) were used for the fluorophore mixtures compared to perylene, which generated wider and stronger Rayleigh scatter bands. These were more difficult to correct because of the increased shot noise, and was best seen in the VV data as Rayleigh scatter is very strongly polarized (SI Fig. S-19). Here after scatter correction, significant residual scatter was observed all along the Rayleigh band which correlated with the higher LOF obtained for VV dataset.

Using this finalised set of constraints, the best MCR model used for anisotropy calculations, were built for each polarized dataset (Figure 5). The first component corresponded to Erythrosin B ($\lambda_{ex/em}$ max = 530/548 nm) and the second to Phloxine B ($\lambda_{ex/em}$ max = 540/554 nm). Some slight deviations were observed between excitation loadings and real components (deviations slightly higher for bilinear model compared to trilinear), but the emission loadings overlapped perfectly with the real spectra. Component 1 explained more variance in the VV data compared to other polarization settings (Table 6) which was because

This is the author version, final accepted draft, but not proof corrected.

Erythrosin B had a larger anisotropy (r = 0.243) than Phloxine B (r = 0.054) because of its much shorter fluorescence lifetime, 75 ps vs. ~1 ns. We are assuming that because both fluorophores have similar molecular masses, and structures, that they will also have similar rotational correlation times in this solvent system [1]. Erythrosin B was thus less depolarized and has stronger emission intensity in the VV configuration. Component 1 deviated slightly from linearity, which was due to the small self-absorption IFE mentioned above, and the effects was largest in the VV configuration. MCR scores (Figure 5) showed that component 2 (PB) varied linearly in all configurations, indicating that there was no detectable IFE or FRET. This was expected because Phloxine B concentration was an order of magnitude lower than Erythrosin B.
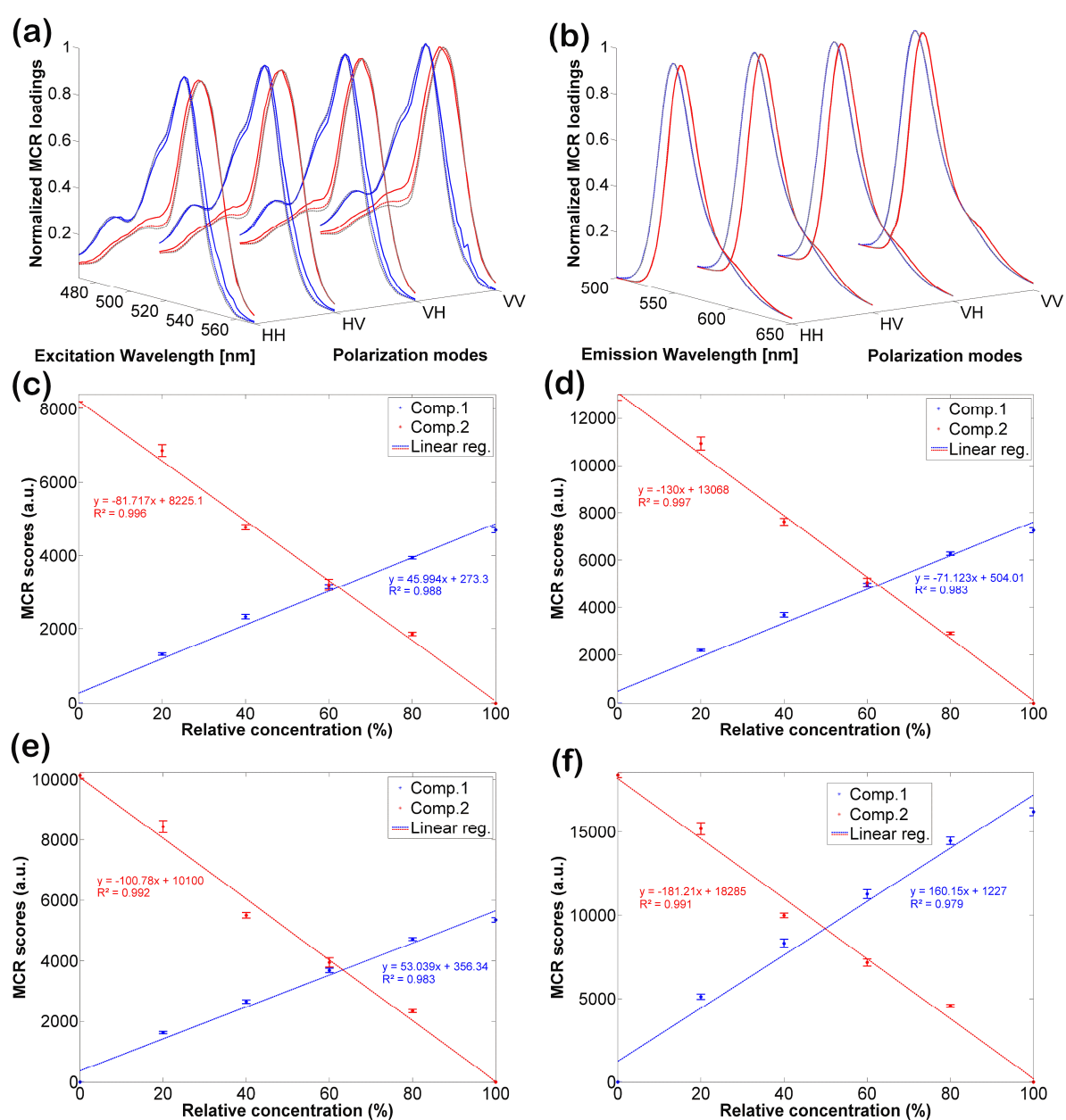
This is the author version, final accepted draft, but not proof corrected.

Figure 5: (Top row) Overlap between real excitation/emission spectra (full line- red/blue) and spectra loadings obtained from EB-PB-EEM-126 model (dash-grey line) and EB-PB-EEM-1256 model (dash-red/blue); (middle & bottom rows) MCR scores obtained for each pure component (EB-PB-EEM-1256 model) for the HH (c), HV (d), VH (e), and VV (f) dataset.

We then used the data from the best model to calculate individual component anisotropy. We first extracted the *aniso*-EEM plots for each resolved component for all mixtures (see Fig. S-20, SI, for some examples). It appeared that the *aniso*-EEM plots in case of mixtures were smooth and uniform for both compounds over the full S_1 emission band region ($\lambda_{ex/em}$ = 520–620/470–570 nm), and correlated well with the data from the pure fluorophore solutions. By averaging the data across the entire S_1 region, a very good agreement was obtained between recovered anisotropy (calculated from the recovered components) and values from pure EB and PB in solution (Table 7), confirming that ARMES could retrieve accurately the anisotropy values of pure fluorophores in mixture, without any rotational ambiguities. We quantified the degree of similarity between pure and recovered *aniso*-EEM plots using a similarity index [45] (Figure 6). Due to variations in the size of the *aniso*-EEM plots between samples (because of the 10% threshold setting [36]), we calculated the similarity index using a specified area that was the same for all samples and contained no NaN valued data points (Fig S-21, SI).

Table 7: Real and modelled (calculated from MCR components) averaged anisotropy values (EB-PB-EEM-1256 model, with the trilinear constraint), for each mixture concentrations, across the S_1 ($\lambda_{ex/em}$) = 520–620/470–570 nm bands.

	Modelled anisotropy ± **STD**	
	Component 1 (EB)	**Component 2 (PB)**
Pure PB EB solutions, real anisotropy values.	**0.243 ± 0.002**	**0.054 ± 0.002**
0% / 100%	/	*0.049 ± 0.001*
20% / 80%	0.244 ± 0.006	0.043 ± 0.001
40% / 60%	0.246 ± 0.004	0.045 ± 0.002
60% / 40%	0.238 ± 0.003	0.048 ± 0.002
80% / 20%	0.234 ± 0.002	0.070 ± 0.008
100% / 0%	*0.241 ± 0.003*	/
Avg/std	0.241 ± 0.005	0.051 ± 0.011

For EB, an index of >0.90 for most samples indicates that the recovered components for all polarization configurations were good and that the recovered *aniso*-EEM plots were accurate (to within ±4%). We also note that the agreement was marginally better for the trilinear model, confirming that trilinear model was slightly better at recovering the anisotropy values. However, for PB, because of its much weaker absorption, the excitation loadings differed slightly from real spectra at wavelengths below 520 nm (Figure 5). The lower magnitude anisotropy of PB (~22% of the EB value) also makes accurate anisotropy component recovery in all polarization configurations a more challenging task, because shot noise from the second fluorophore will cause significant problems as seen in Figure 6b where the difference between real and recovered *aniso*-EEM plots gets larger and larger as the

proportion of EB fluorescence (and its constituent shot noise) increases. All of these effects resulted in less accurate recovered anisotropies (~±20% of real value) and the similarity index only gave good values for $\lambda_{ex} > 520$ nm, where absorbance was greatest (Figure S-21, SI).
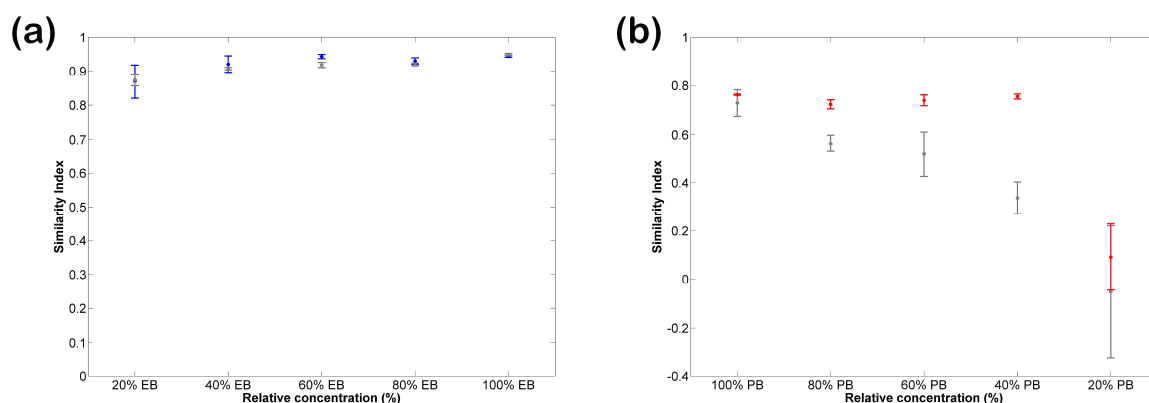

Figure 6: Similarity indices calculated between anisotropy plot extracted from real pure compounds in solution, and the recomposed components. (Left) Results for EB, with results from trilinear model (blue) and bilinear model (grey), (Right) Data for PB, with results from the trilinear (red) and bilinear models (grey).

4. Conclusions

These results show that it is possible to accurately extract the anisotropy of individual components using MCR from relatively simple small molecule fluorophore mixtures once appropriate data organisation and constraints have been applied. For TSFS data, SWA with non-negativity, and unimodality constraints generates sufficiently accurate anisotropy data. Overall, however, MCR modelling of TSFS data was less efficient than MCR modelling of EEM data which was, for example better able to cleanly resolve the impurity in the perylene solutions. For the EEM-MCR modelling the optimal settings were to use normalization, non-negativity, and total trilinearity constraints, with correspondence among species being required for mixtures where the species had similar emission intensities. Recovery of component anisotropy via chemometric modelling was also achieved and was accurate to ±4% for relatively large magnitude anisotropies (*e.g.* Perylene S_1 and EB). For the lower magnitude anisotropy (<0.06) fluorophores accuracy decreased (±20%) due to the impact of shot noise from the overlapping other component and relative measurement error. This might be rectified, by changing the measurement conditions to improve signal to noise, which should result in less variation in the recovered components and thus the calculated anisotropies. Despite this, the fact that these very low anisotropy components were recovered was still very significant.

Being able to recover the spectral and anisotropy information using MCR with either TSFS or EEM measurements provides a useful tool for accurately characterizing molecular systems where the fluorophores are not interacting (FRET or IFE) with each other and where significant size, mobility, or lifetime changes are occurring (*e.g.* fluorophore diffusion in polymer matrixes). The two sample systems used here also provide very simple and robust test systems for validating the TSFS/EEM measurements and chemometric data analysis elements

This is the author version, final accepted draft, but not proof corrected.

of ARMES. The next stage is to see if it is feasible to analyze/model much more complex situations where fluorophores have FRET interactions, such as the case with proteins.

5. Supplemental information available
Supporting information is available and includes further details about the spectral measurements and the chemometric modelling.

Acknowledgements

References:
[1] J.R. Lakowicz, Principles of Fluorescence Spectroscopy, 3rd Edition ed., Springer, New York, 2006.
[2] I.B. Bekard, D.E. Dunstan, Tyrosine Autofluorescence as a Measure of Bovine Insulin Fibrillation, Biophys. J., 97 (2009) 2521-2531.
[3] D.M. Togashi, A.G. Ryder, D. O'Shaughnessy, Monitoring local unfolding of bovine serum albumin during denaturation using steady-state and time-resolved fluorescence spectroscopy, J Fluoresc, 20 (2010) 441-452.
[4] E. Lissi, C. Calderon, A. Campos, Evaluation of the Number of Binding Sites in Proteins from their Intrinsic Fluorescence: Limitations and Pitfalls, Photochem. Photobiol., 89 (2013) 1413-1416.
[5] K. Sagoo, R. Hirsch, P. Johnston, D. McLoskey, G. Hungerford, Pre-denaturing transitions in human serum albumin probed time-resolved phosphorescence using, Spectrochimica Acta Part A-Molecular And Biomolecular Spectroscopy, 124 (2014) 611-617.
[6] E.A. Burstein, N.S. Vedenkin, M.N. Ivkova, Fluorescence and the Location of Tryptophan Residues in Protein Molecules, Photochem. Photobiol., 18 (1973) 263-279.
[7] N. Tayeh, T. Rungassamy, J.R. Albani, Fluorescence spectral resolution of tryptophan residues in bovine and human serum albumins, J. Pharm. Biomed. Anal., 50 (2009) 107-116.
[8] I.M. Warner, G.D. Christian, E.R. Davidson, J.B. Callis, Analysis of Multicomponent Fluorescence Data, Anal. Chem., 49 (1977) 564-573.
[9] D. Patra, A.K. Mishra, Recent developments in multi-component synchronous fluorescence scan analysis, Trac-Trends in Analytical Chemistry, 21 (2002) 787-798.
[10] R.B. Thompson, B.P. Maliwal, C.A. Fierke, Expanded dynamic range of free zinc ion determination by fluorescence anisotropy, Analytical Chemistry, 70 (1998) 1749-1754.
[11] B. Li, P.W. Ryan, M. Shanahan, K.J. Leister, A.G. Ryder, Fluorescence EEM Spectroscopy for Rapid Identification and Quality Evaluation of Cell Culture Media Components., Appl. Spectrosc., 65 (2011) 1240-1249.
[12] B. Li, M. Shanahan, A. Calvet, K.J. Leister, A.G. Ryder, Comprehensive, quantitative bioprocess productivity monitoring using fluorescence EEM spectroscopy and chemometrics, Analyst, 139 (2014) 1661-1671.
[13] J.H. Jiang, Y. Ozaki, Self-modeling curve resolution (SMCR): Principles, techniques, and applications, Appl. Spectrosc. Rev., 37 (2002) 321-345.
[14] M.C.G. Antunes, J. da Silva, Multivariate curve resolution analysis excitation-emission matrices of fluorescence of humic substances, Anal. Chim. Acta, 546 (2005) 52-59.
[15] J.C.G.E. da Silva, R. Tauler, Multivariate curve resolution of synchronous fluorescence spectra matrices of fulvic acids obtained as a function of pH, Appl. Spectrosc., 60 (2006) 1315-1321.

This is the author version, final accepted draft, but not proof corrected.

[16] A. de Juan, R. Tauler, Multivariate curve resolution (MCR) from 2000: Progress in concepts and applications, Crit. Rev. Anal. Chem., 36 (2006) 163-176.

[17] R. Bro, PARAFAC. Tutorial and applications, Chemom. Intell. Lab. Syst., 38 (1997) 149-171.

[18] C.M. Andersen, R. Bro, Practical aspects of PARAFAC modeling of fluorescence excitation-emission data, J. Chemom., 17 (2003) 200-215.

[19] H. Chen, J.E. Kenny, Application of PARAFAC to a two-component system exhibiting Fluorescence Resonance Energy Transfer: from theoretical prediction to experimental validation, Analyst, 137 (2012) 153-162.

[20] Å. Rinnan, K.S. Booksh, R. Bro, First order Rayleigh scatter as a separate component in the decomposition of fluorescence landscapes, Analytica Chimica Acta, 537 (2005) 349-358.

[21] R.D. JiJi, K.S. Booksh, Mitigation of Rayleigh and Raman spectral interferences in multiway calibration of excitation-emission matrix fluorescence spectra, Anal. Chem., 72 (2000) 718-725.

[22] A. Rinnan, C.M. Andersen, Handling of first-order Rayleigh scatter in PARAFAC modelling of fluorescence excitation-emission data, Chemom. Intell. Lab. Syst., 76 (2005) 91-99.

[23] K.R. Murphy, C.A. Stedmon, D. Graeber, R. Bro, Fluorescence spectroscopy and multi-way techniques. PARAFAC, Analytical Methods, 5 (2013) 6557-6566.

[24] K. Kumar, A.K. Mishra, Multivariate curve resolution alternating least square (MCR-ALS) analysis on total synchronous fluorescence spectroscopy (TSFS) data sets: Comparing certain ways of arranging TSFS-based three-way array, Chemom. Intell. Lab. Syst., 147 (2015) 66-74.

[25] R. Tauler, I. Marques, E. Casassas, Multivariate curve resolution applied to three-way trilinear data: Study of a spectrofluorimetric acid–base titration of salicylic acid at three excitation wavelengths, Journal of Chemometrics, 12 (1998) 55-75.

[26] K. Kumar, A.K. Mishra, Application of 'multivariate curve resolution alternating least square (MCR–ALS)' analysis to extract pure component synchronous fluorescence spectra at various wavelength offsets from total synchronous fluorescence spectroscopy (TSFS) dataset of dilute aqueous solutions of fluorophores, Chemometrics and Intelligent Laboratory Systems, 116 (2012) 78-86.

[27] C.A. Parker, W.T. Rees, Fluorescence spectrometry. A review, Analyst, (1962) 83-111.

[28] A.C. Olivieri, Chapter 14. Application Example: U-PLS/RBL, Practical three-way calibration, ElsevierEscandar, G. M.

[29] A. de Araujo Gomes, A.V. Schenone, H.C. Goicoechea, M.C.U. de Araujo, Unfolded partial least squares/residual bilinearization combined with the Successive Projections Algorithm for interval selection: enhanced excitation-emission fluorescence data modeling in the presence of the inner filter effect, Analytical Bioanalytical Chemistry, 407 (2015) 5649-5659.

[30] G.N. Piccirilli, G.M. Escandar, Partial least-squares with residual bilinearization for the spectrofluorimetric determination of pesticides. A solution of the problems of inner-filter effects and matrix interferents, Analyst, 131 (2006) 1012-1020.

[31] L. Lakhal, V. Acha, T. Aussenac, PARAFAC analysis of front-face fluorescence data: Absorption and scattering effects assessed by means of Monte Carlo simulations, Chemometrics and Intelligent Laboratory Systems, 116 (2012) 112-122.

[32] M.E. Pacheco, L. Bruzzone, Synchronous fluorescence spectrometry: Conformational investigation or inner filter effect?, Journal of Luminescence, 137 (2013) 138-142.

[33] T. Forster, Intermolecular energy migration and fluorescence, Annalen der physik, 2 (1948) 55-75.

[34] R.C. Groza, A. Calvet, A.G. Ryder, A fluorescence anisotropy method for measuring protein concentration in complex cell culture media, Anal. Chim. Acta, 821 (2014) 54-61.

[35] R.C. Groza, B. Li, A.G. Ryder, Anisotropy resolved multidimensional emission spectroscopy (ARMES): A new tool for protein analysis, Anal. Chim. Acta, 886 (2015) 133-142.

This is the author version, final accepted draft, but not proof corrected.

[36] Y. Casamayou-Boucau, A.G. Ryder, Extended wavelength Anisotropy Resolved Multidimensional Emission Spectroscopy (ARMES) measurements: better filters, validation standards, and Rayleigh scatter removal methods, Methods Appl Fluoresc, (2017).

[37] J.B.-A. Johansson, Limiting Fluorescence Anisotropies of Perylene and Xanthene Derivatives, Journal of the Chemical Society, Faraday Transactions, 86 (1990) 2103-2107.

[38] T.J.V. Prazeres, A. Fedorov, S.P. Barbosa, J.M.G. Martinho, M.N. Berberan-Santos, Accurate determination of the limiting anisotropy of rhodamine 101. Implications for its use as a fluorescence polarization standard, J. Phys. Chem. A, 112 (2008) 5034-5039.

[39] M.D. Barkley, A.A. Kowalczyk, L. Brand, Fluorescence decay studies of anisotropic rotations of small molecules, The Journal of Chemical Physics, 75 (1981) 3581-3593.

[40] J. Jaumot, A. de Juan, R. Tauler, MCR-ALS GUI 2.0: New features and applications, Chemometrics and Intelligent Laboratory Systems, 140 (2015) 1-12.

[41] R.C. Groza, Anisotropy Resolved Multi-dimensional Emission Spectroscopy (ARMES): A new tool for the quantitative and structural analysis of proteins., Chemistry, National University of Ireland Galway, Galway, Ireland, 2016.

[42] J. Jaumot, R. Gargallo, A. de Juan, R. Tauler, A graphical user-friendly interface for MCR-ALS: a new tool for multivariate curve resolution in MATLAB, Chemom. Intell. Lab. Syst., 76 (2005) 101-110.

[43] J. Jaumot, R. Tauler, MCR-BANDS: A user friendly MATLAB program for the evaluation of rotation ambiguities in Multivariate Curve Resolution, Chemom. Intell. Lab. Syst., 103 (2010) 96-107.

[44] W. Windig, J. Guilment, Interactive Self-Modeling Mixture Analysis, Analytical Chemistry, 63 (1991) 1425-1432.

[45] B. Li, A.G. Ryder, Similarity index: a rapid classification method for multivariate data arrays., National University of Ireland, Galway (Galway, IE, United States, 2009.

[46] Y. Casamayou-Boucau, A.G. Ryder, Extended wavelength anisotropy resolved multidimensional emission spectroscopy (ARMES) measurements: better filters, validation standards, and Rayleigh scatter removal methods, Methods Appl Fluoresc, 5 (2017) 037001.

[47] A. Gaiduk, P.V. Ruijgrok, M. Yorulmaz, M. Orrit, Making gold nanoparticles fluorescent for simultaneous absorption and fluorescence detection on the single particle level, Physical Chemistry Chemical Physics, 13 (2001) 149-153.

[48] S. Freire, M.H. de Araujo, W. Al-Soufi, M. Novo, Photophysical study of Thioflavin T as fluorescence marker of amyloid fibrils, Dyes and Pigments, 110 (2014) 97-105.

[49] A. Gafni, L. Brand, Fluorescence decay studies of reduced nicotinamide adenine dinucleotide in solution and bound to liver alcohol dehydrogenase, Biochemistry 15 (1976) 3165-3171.

[50] A. de Juan, R. Tauler, Chemometrics applied to unravel multicomponent processes and mixtures: Revisiting latest trends in multivariate resolution, Analytica Chimica Acta, 500 (2003) 195-210.

[51] A. de Juan, R. Tauler, Comparison of three-way resolution methods for non-trilinear chemical data sets, Journal of CHemometrics, 15 (2001) 749-771.

[52] R. Tauler, A. Smilde, B. Kowalski, Selectivity, local rank, three-way data analysis and ambiguity in multivariate curve resolution, Journal of Chemometrics, 9 (1995) 31-58.

[53] R.B. Thompson, I. Gryczynski, J. Malicka, Fluorescence Polarization Standards for High-Throughput Screening and Imaging, Biotechniques, 32 (2002) 34-42.

[54] A. Matczuk, P. Bojarski, I. Gryczyński, J. Kuśba, L. Kułak, C. Bojarski, The influence of water structure on the rotational depolarization of fluorescence, Journal of Photochemistry and Photobiology A: Chemistry, 90 (1995) 91-94.